

Bubbly flow in an airlift column: a CFD study

Liao, J.; Ziegenhein, T.; Rzehak, R.;

Originally published:

March 2016

Journal of Chemical Technology & Biotechnology 91(2016), 2904-2915

DOI: <https://doi.org/10.1002/jctb.4917>

Perma-Link to Publication Repository of HZDR:

<https://www.hzdr.de/publications/Publ-23289>

Release of the secondary publication
on the basis of the German Copyright Law § 38 Section 4.

Bubbly flow in an airlift column: a CFD study

Jing Liao, Thomas Ziegenhein, Roland Rzehak

Helmholtz-Zentrum Dresden - Rossendorf,

Institute of Fluid Dynamics, P.O. Box 510119 D-01314 Dresden, Germany

Abstract

BACKGROUND: Multiphase CFD (Computational Fluid Dynamics) simulation is a valuable tool in chemical and bioprocess engineering that is particularly useful to study reactor concepts and their scale-up from laboratory to production scale. Simulations of bubbly flows up to industrial dimensions are feasible within the Eulerian two-fluid framework of interpenetrating continua. However, for practical applications suitable closure models are needed which describe the physics on the scale of individual bubbles or groups thereof. The quest for such models with a broad range of applicability allowing predictive simulations is an ongoing venture.

RESULTS: A set of closure relations for the fluid dynamics of bubbly flow has been collected that represents the best available knowledge and may serve as a baseline for further improvements and extensions. This model has been successfully validated for bubbly flows in pipes and bubble columns. Here it is applied to the case of an internal loop airlift column which is frequently used in biotechnological processes.

CONCLUSION: Within the limitations of the experimental data available for comparison, the closures are found applicable to this case as well. Further development should account for the polydisperse nature of the flow. To this end reliable measurements of bubble size distribution are needed.

Keywords: bio-process engineering, internal loop airlift column, dispersed gas liquid multiphase flow, Euler Euler two fluid model, closure relations, CFD simulation

1 INTRODUCTION

Bubbly flows are common in biotechnological applications where they provide feed and removal of gaseous nutrients and metabolites as well as mechanical agitation to mix the fermentation broth and keep the microorganisms suspended. The development of biotechnological processes is often difficult because several partly conflicting requirements must be met simultaneously. For example in addition to ensure sufficient transport of nutrients and metabolites, temperature and pH must be kept in a rather narrow range and the mechanical stress exerted on the microorganisms must remain low. A typical problem that arises in this context is that the mechanical power supplied in order to provide mixing and mass-transfer goes along with high shear rates which cause damage to the cells. ¹ On the small laboratory scales the bioreactor may be considered as well mixed and working solutions are relatively easy to find. On the large production scales, however, the system is inhomogeneous and fluid dynamical effects become important. ² Consequently scale-up requires adjustments beyond simple geometric enlargement and represents a complex optimization problem. ³ In this situation CFD simulations are a helpful tool of growing importance for both analysis and prediction. ⁴⁻⁷

A bioreactor configuration that is frequently used in biotechnological applications is the airlift-column. ⁸ Different types of construction may be distinguished, namely split columns, columns with internal draft tube, and external loop columns. ⁹ Compared to the similar bubble column, the airlift column provides better mixing at rather low power input but is geometrically more complex. ¹⁰ For example the performance of an airlift column with internal draft tube is known to be affected by the cross-sectional area ratio of riser and downcomer, ¹¹ bottom and top clearances ¹²⁻¹⁴ as well as the design of base, sparger and separator ¹⁵⁻¹⁷ in addition to operational parameters such as the gas flow. Therefore, CFD

simulations offer good opportunities for bioreactor optimization, but a computational model is needed that applies to all geometric variants alike.

Multiphase CFD simulations on the scale of technical equipment become feasible within the purely Eulerian framework of interpenetrating continua.¹⁸⁻²⁰ In this approach an averaging procedure is invoked to eliminate the small length scales associated with the phase interface so that simulation on domains of the large size of the equipment becomes feasible. However, for practical applications the physical phenomena taking place on the scale of individual bubbles or groups thereof have to be modeled by suitable closure relations. Thorough validation of these closure models is a cornerstone on the way to achieve reliable predictions. A complete model is very complex comprising the processes of mixing,²¹ mass transfer,²² metabolism,²³ and for phototrophic organisms in addition light transmission²⁴ coupled to the fluid dynamics. To obtain reliable results in this situation each part of the model has to be validated individually.

Even when attention is confined to the purely fluid dynamical part of the problem a large number of works exist, in each of which largely a different set of closure relations is compared to a different set of experimental data. Examples of such approaches are abundant for bubble columns²⁵⁻²⁷ and bubbly pipe flow.²⁸⁻³⁰ For the limited range of conditions to which each model variant is applied, reasonable agreement with the data is mostly obtained, but due to a lack of comparability between the individual works no complete, reliable, and robust formulation has emerged so far. Moreover, the models usually contain a number of empirical parameters that have been adjusted to match the particular data that were used in the comparison. Predictive simulation, however, requires a model that works without any adjustments within the targeted domain of applicability.

Airlift-columns in contrast have received comparatively less attention in simulation studies. Recent simulations of bubbly flow in the internal loop type are given in Refs. 31-38. In most

of these studies comparison to experiment has been made only for integral data like the total gas holdups in riser and downcomer or the average liquid circulation velocity. This only provides a limited validation of the closure models used. Notable exceptions are the works of Luo³⁴ and Talvy et al.³⁵, in which local measurements have been considered like radial profiles of gas fraction and liquid velocity taken at different heights. In part of the works only axisymmetric 2D flows have been considered. Comparisons of 2D and 3D simulations are provided in Refs. 31-32 and 34-35 in which some differences were seen but not very large. From the foregoing discussion it becomes clear that for the fluid dynamics of bubbly flow in airlift columns a model that is well validated for a sufficiently broad range of conditions including geometric variations does not exist to date. In the present contribution a step towards this goal is taken by applying a baseline closure model that was previously shown to work reasonably well for bubbly flows in pipes and bubble columns of different size and shape³⁹⁻⁴³ to an airlift column with internal draft tube. This configuration has been chosen because a set of experimental data³⁴ is available which comprises spatially resolved measurements of gas fraction, liquid velocity and turbulent kinetic energy that allow to validate the model.

The idea of the baseline model approach is that the same closure model should be applicable to all systems where the small scales are governed by the same physics. For the fluid dynamics of monodisperse bubbly flows the best available description for the aspects known to be relevant has been collected from the literature with some gaps filled by comparison of different plausible alternatives.^{39, 44} In this case closure is required for (i) the exchange of momentum between liquid and gas phases, and (ii) the effects of the dispersed bubbles on the turbulence of the liquid carrier phase. Apart from interest in its own right, results obtained for this restricted problem also provide a good starting point for the investigation of more complex situations as described above.

Restriction to situations in which a fixed distribution of bubble sizes may be imposed bypasses the additional complexity of modelling bubble coalescence and breakup processes. This facilitates as a first step the validation of the other parts of the overall model. Once this is accomplished the validity of models for bubble-coalescence and -breakup may be assessed in a second step on the basis of the previously qualified models for bubble forces and bubble-induced turbulence.

The paper is organized as follows. In section 2 a summary of the experimental data of Luo³⁴ is given. The closure relations for bubble forces and bubble-induced turbulence are described in section 3 together with other relevant aspects of the overall model. In section 4 we present the main comparison between simulation results and experimental data considering several simulation setups while in section 5 discussion and conclusion are offered.

2 SUMMARY OF EXPERIMENTAL DATA

Luo³⁴ has presented data on air / water bubbly flow in an internal loop airlift column. From this work one test case has been selected for which detailed local measurements were taken that are suitable for the validation of CFD models. The geometry is sketched in Fig. 1. The airlift column consists of a round container with 130 mm inner diameter into which a 1050 mm long draft tube of 80 mm inner diameter and 5 mm wall thickness is inserted. The distance of the lower end of the draft tube from the bottom of the column is 50 mm. The distance of the upper end of the draft tube from the static water level, i.e. the water level without any gas present, is 30 mm. Gas is supplied through a ring sparger of 25 mm inner diameter located 25 mm above the column bottom which is made of a tube with 5 mm outer diameter which has an upward facing hole of 1 mm diameter every 24°. The static water level is at 1130 mm. The average gas volume flux through the entire cross section of the container is $J_G = 0.01$ m/s. A total gas hold-up of ~3% has been measured. From this, the dynamic water level is calculated as 1160 mm. Since this value determines the domain for the simulations it is used in Fig. 1.

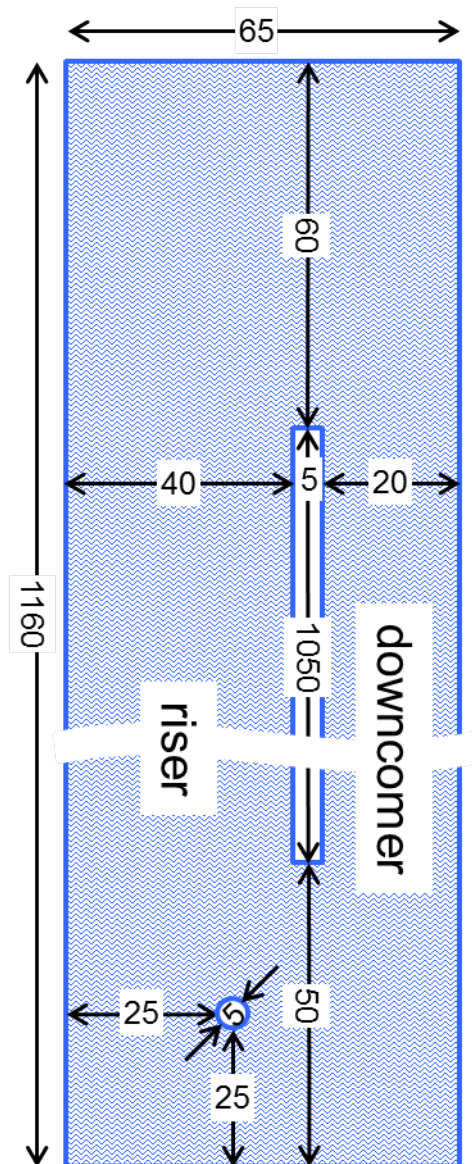


Figure 1: Axial section showing half of the column with the centerline on the left and the container wall on the right up to the dynamic water level. All sizes are given in mm.

Two types of measurement have been performed. Radial profiles of the time-averaged gas fraction have been measured by γ -ray tomography at five different heights in the column as listed in Table 1. The liquid velocity has been determined by Computer-Automated Radioactive Particle Tracking (CARPT). Radial profiles of both the time-averaged axial

velocity and turbulent kinetic energy are available which have been averaged over the portion of the column between 300 and 800 mm height, where the flow is developed in the sense that no variations in the axial direction occur. The density of the tracer particle has been matched to that of the water used as carrier liquid but due to the rather large size of the particle (0.8 mm diameter) some deviation between the true liquid velocity and the measured velocity of the tracer particle may still exist in particular concerning the fast small-scale turbulent fluctuations.

For the bubble size a value of 3 mm is given, but it is not explained how this value has been obtained, so that it can only be considered as a rough estimate. It must be noted that in particular simple inspection of the column from the outside may give grossly wrong results for the average bubble size. For example lift forces (see section 3.2) may result in a tendency of smaller bubbles to accumulate near the walls while larger bubbles are depleted in this region. Especially in the downcomer which is seen from the outside only the smaller bubbles are expected because the larger bubbles in the riser likely exit the column immediately when reaching the top.^{45,8} Since the origin of the reported value is not known and its reliability cannot be judged, the bubble size will be treated as a parameter in the simulations.

level			H1	H2	H3	H4	H5
height	<i>H</i>	[mm]	42	342	677	977	1100

Table 1: Heights for gas fraction measurements.

2 DESCRIPTION OF MODELS

The conservation equations of the Euler-Euler two-fluid model have been discussed at length in a number of books¹⁸⁻²⁰ and a broad consensus has been reached, so this general framework will not be repeated here. Closure relations required to complete the model, in contrast, are still subject to considerable variation between researchers. Here, the baseline model that has emerged from previous work^{44, 46, 39, 41,42} is adopted. This model has been validated for a number of different test cases including bubbly flow in pipes and bubble columns. Details of the model are given in section 3.1 for the bubble forces and in section 3.2 for bubble-induced turbulence. Other aspects of the models are specified in section 3.3, namely bubble size, boundary conditions and geometry.

2.1 Bubble Forces

Concerning momentum exchange between liquid and gas phase drag, lift, wall, and turbulent dispersion forces are considered in the baseline model. The virtual mass force has been neglected initially but is shown in the end to have only minor effects. The correlations are expressed in terms of the dimensionless numbers, namely the Reynolds number $Re = |\mathbf{u}_G - \mathbf{u}_L| d_b \nu_L^{-1}$, the Eötvös number $Eo = (\rho_L - \rho_G) g d_b^2 \sigma^{-1}$, and the Morton number $Mo = (\rho_L - \rho_G) \rho_L^2 g \nu_L^4 \sigma^{-3}$.

2.1.1 Drag Force

The drag force reflects the resistance opposing bubble motion relative to the surrounding liquid. The corresponding gas-phase momentum source is given by

$$\mathbf{F}^{drag} = -\frac{3}{4d_B} C_D \rho_L \alpha_G |\mathbf{u}_G - \mathbf{u}_L| (\mathbf{u}_G - \mathbf{u}_L) . \quad (1)$$

The drag coefficient C_D depends strongly on the Reynolds number Re and for deformable bubbles also on the Eötvös number Eo . A correlation distinguishing different shape regimes has been suggested by Ishii and Zuber⁴⁷, namely

$$C_D = \max(C_{D,sphere}, \min(C_{D,ellipse}, C_{D,cap})) , \quad (2)$$

where

$$\begin{aligned} C_{D,sphere} &= \frac{24}{Re} (1 + 0.1 Re^{0.75}) \\ C_{D,ellipse} &= \frac{2}{3} \sqrt{Eo} \\ C_{D,cap} &= \frac{8}{3} \end{aligned} . \quad (3)$$

This correlation was compared with an extensive data set on the terminal velocity of bubbles rising in quiescent liquids covering several orders of magnitude for each of Re , Eo and Mo by Tomiyama et al.⁴⁸ with good agreement except at high values of Eo .

2.1.2 Lift Force

A bubble moving in an unbounded shear flow experiences a force perpendicular to the direction of its motion. The momentum source corresponding to this shear lift force, often simply referred to as lift force, can be calculated as: ⁴⁹

$$\mathbf{F}^{lift} = -C_L \rho_L \alpha_G (\mathbf{u}_G - \mathbf{u}_L) \times rot(\mathbf{u}_L) . \quad (4)$$

For a spherical bubble the shear lift coefficient C_L is positive so that the lift force acts in the direction of decreasing liquid velocity, i.e. in case of co-current pipe flow in the direction towards the pipe wall. Experimental ⁵⁰ and numerical ⁵¹ investigations showed, that the direction of the lift force changes its sign if a substantial deformation of the bubble occurs. From the observation of the trajectories of single air bubbles rising in simple shear flow of a glycerol water solution the following correlation for the lift coefficient was derived: ⁵⁰

$$C_L = \begin{cases} \min[0.288 \tanh(0.121 \text{Re}), f(Eo_{\perp})] & Eo_{\perp} < 4 \\ f(Eo_{\perp}) & \text{for } 4 < Eo_{\perp} < 10 \\ -0.27 & 10 < Eo_{\perp} \end{cases} . \quad (5)$$

with $f(Eo_{\perp}) = 0.00105 Eo_{\perp}^3 - 0.0159 Eo_{\perp}^2 - 0.0204 Eo_{\perp} + 0.474$

This coefficient depends on the modified Eötvös number given by

$$Eo_{\perp} = \frac{g(\rho_L - \rho_G)d_{\perp}^2}{\sigma} , \quad (6)$$

where d_{\perp} is the maximum horizontal dimension of the bubble. It is calculated using an empirical correlation for the aspect ratio by ⁵² with the following equation:

$$d_{\perp} = d_B \sqrt[3]{1 + 0.163 Eo^{0.757}}, \quad (7)$$

where Eo is the usual Eötvös number. The resulting bubble size dependence of the lift coefficient for air bubble in water is shown in Fig. 2 from which the change in sign is seen to occur at a bubble size of $d_B \approx 6$ mm.

The experimental conditions on which Eq. (5) is based, were limited to the range $-5.5 \leq \log_{10} Mo \leq -2.8$, $1.39 \leq Eo \leq 5.74$ and values of the Reynolds number based on bubble diameter and shear rate $0 \leq Re \leq 10$. The water-air system at normal conditions has a Morton number $Mo = 2.63 \cdot 10^{-11}$ which is quite different, but good results have nevertheless been reported for this case.⁵³

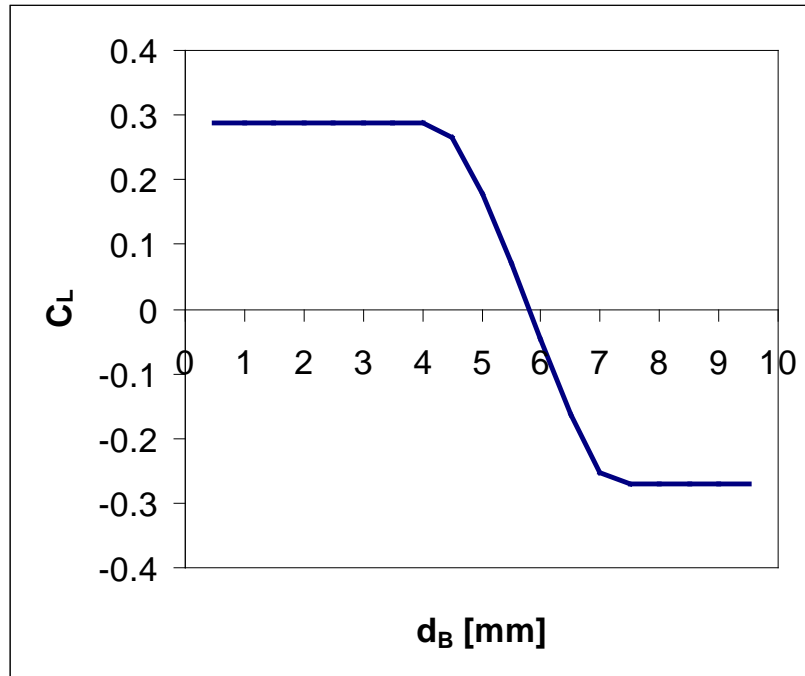


Figure 2: Dependence of the lift coefficient C_L on the bubble size d_B for air bubbles in water according to Eqs. (6) – (8).

2.1.3 Wall Force

A bubble translating next to a wall in an otherwise quiescent liquid also experiences a lift force. This wall lift force, often simply referred to as wall force, has the general form

$$\mathbf{F}^{wall} = \frac{2}{d_B} C_W \rho_L \alpha_G |\mathbf{u}_G - \mathbf{u}_L|^2 \hat{\mathbf{y}}, \quad (8)$$

where $\hat{\mathbf{y}}$ is the unit normal perpendicular to the wall pointing into the fluid. The dimensionless wall force coefficient C_W depends on the distance to the wall y and is expected to be positive so the bubble is driven away from the wall.

Based on the observation of single bubble trajectories in simple shear flow of a glycerol water solution Tomiyama et al.⁵⁴ and later Hosokawa et al.⁵⁵ concluded a functional dependence

$$C_W(y) = f(Eo) \left(\frac{d_B}{2y} \right)^2. \quad (9)$$

In the limit of small Morton number the correlation

$$f(Eo) = 0.0217 Eo \quad (10)$$

can be derived from the data of Hosokawa et al.⁵⁵. The experimental conditions on which Eq. (11) is based are $2.2 \leq Eo \leq 22$ and $-6.0 \leq \log_{10} Mo \leq -2.5$ which is still different from the

water-air system with $Mo = 2.63 \cdot 10^{-11}$ but a recent investigation of Rzehak et al. ⁴⁴ has nonetheless shown that good predictions are obtained also for air bubbles in water.

2.1.4 Turbulent Dispersion Force

The turbulent dispersion force describes the effect of the turbulent fluctuations of liquid velocity on the bubbles. Burns et al. (2004) ⁵⁶ derived an explicit expression by Favre averaging the drag force as:

$$\mathbf{F}^{disp} = -\frac{3}{4} C_D \frac{\alpha_G}{d_B} |\mathbf{u}_G - \mathbf{u}_L| \frac{\mu_L^{turb}}{\sigma_{TD}} \left(\frac{1}{\alpha_L} + \frac{1}{\alpha_G} \right) \text{grad } \alpha_G. \quad (11)$$

In analogy to molecular diffusion, σ_{TD} is referred to as a Schmidt number. In principle it should be possible to obtain its value from single bubble experiments also for this force by evaluating the statistics of bubble trajectories in well characterized turbulent flows but to our knowledge this has not been done yet. A value of $\sigma_{TD} = 0.9$ is typically used.

In the same work the expression for the so-called Favre averaged drag (FAD) model has also been compared with other suggestions which all agree at least in the limit of low void fraction.

2.1.5 Virtual Mass Force

When a bubble is accelerated, a certain amount of liquid has to be set into motion as well. This may be expressed as a force acting on the bubble as

$$\mathbf{F}^{VM} = -C_{VM} \rho_L \alpha_G \left(\frac{D_G \mathbf{u}_G}{Dt} - \frac{D_L \mathbf{u}_L}{Dt} \right), \quad (12)$$

where D_G / Dt and D_L / Dt denote material derivatives with respect to the velocity of the indicated phase. For the virtual mass coefficient a value of $C_{VM} = 0.5$ has been derived for isolated spherical bubbles in inviscid⁵⁷ and creeping flows⁵⁸. Results of direct simulations of a single⁵⁹ suggest that this value also holds for intermediate values of Re .

2.2 Two-phase Turbulence

Due to the small density and small special scales of the dispersed gas it suffices to consider turbulence in the continuous liquid phase for bubbly flows. We adopt a two equation turbulence model for the liquid phase with additional source terms describing bubble induced turbulence. The formulation given is equally applicable to either k- ϵ , k- ω or SST model, but the latter⁶⁰ will be used presently.

Concerning the source term describing bubble effects in the k-equation there is large agreement in the literature.^{61,30} A plausible approximation is provided by the assumption that all energy lost by the bubble due to drag is converted to turbulent kinetic energy in the wake flow behind the bubble. Hence, the k-source becomes

$$S_L^k = \mathbf{F}_L^{drag} \cdot (\mathbf{u}_G - \mathbf{u}_L). \quad (13)$$

For the ϵ -source a similar heuristic is used as for the single phase model, namely the k-source is divided by some time scale τ so that

$$S_L^\varepsilon = C_{\varepsilon B} \frac{S_L^k}{\tau} . \quad (14)$$

Further modeling then focuses on the time scale τ proceeding largely based on dimensional analysis. This follows the same line as the standard modeling of shear-induced turbulence in single phase flows (Wilcox 1998),⁶² where production terms in the ε -equation are obtained by multiplying corresponding terms in the k -equation by an appropriate time scale which represents the life-time of a turbulent eddy before it breaks up into smaller structures. In single phase turbulence the relevant variables are obviously k and ε from which only a single time scale $\tau = k_L / \varepsilon_L$ can be formed. For the bubble-induced turbulence in two-phase flows the situation is more complex. Obviously there are two length and two velocity scales in the problem, where one of each is related to the bubble and the other to the turbulent eddies. From these a total of four different time scales can be formed. In the absence of theoretical arguments to decide which of these is the most relevant one, a comparison of all four alternatives³⁹ has shown the best performance for the choice $\tau = d_B / \sqrt{k_L}$ and this is followed herein. For the coefficient $C_{\varepsilon B}$ a value of 1.0 was found to give reasonable results³⁹.

For use with the SST model, the ε -source is transformed to an equivalent ω -source which gives

$$S_L^\omega = \frac{1}{C_\mu k_L} S_L^\varepsilon - \frac{\omega_L}{k_L} S_L^k . \quad (15)$$

This ω -source is used independently of the blending function in the SST model since it should be effective throughout the fluid domain.

Since bubble-induced effects are included in k and ε / ω due to the respective source terms, the turbulent viscosity is evaluated from the standard formula

$$\mu_L^{turb} = C_\mu \rho_L \frac{k_L^2}{\varepsilon_L} . \quad (16)$$

The effective viscosity is simply $\mu_L^{eff} = \mu_L^{mol} + \mu_L^{turb}$.

Boundary conditions on k and ε / ω are taken the same as for the single phase case, which is consistent with the view that the full wall shear stress is exerted by the liquid phase which contacts the full wall area. A single phase wall function is employed to avoid the need to resolve the viscous sublayer.

All turbulence model parameters take their usual single phase values for the presently investigated tests.

3 SIMULATION RESULTS

All simulations have been run using a customized version of ANSYS CFX 14.5. Different setups have been used where the geometry is simplified to different degrees. As seen from the overview of previous simulations of draft tube airlift columns the feasibility of such simplifications is not yet clear. A great speed up of the calculation results when axisymmetric conditions are assumed so that it suffices to consider only a narrow sector of the column. In addition the internals, i.e. draft tube and sparger, may be simplified to planes or points rather than accounting for their true thickness. This gives greater flexibility to choose the grid spacing while maintaining a regular undistorted structure. An overview including the order of grid points and calculation times is given in Table 2.

The first setup is the most simplified where only a quasi-2D domain is considered in which the draft tube appears as a line and the sparger as a point. For the second setup the finite thickness of the draft tube and the extent of the sparger tube have been accounted for. To match with cells of a rectangular grid the cross-section of the sparger tube has been changed to a square. For the third setup, finally, the calculations have been done on the full 3D cylindrical domain.

For each setup a number of refined grids were considered to assess grid-independence of the results. Details of the grid spacing and number of grid points are given in Table 3 below. The finally used grids for setups 2 and 3 are shown in Fig. 3.

Results presented in the following have been obtained without considering the virtual mass force, but it has been verified for the final settings that its effect is indeed small.

setup	dimensionality	internals	grid points / 10 ³	calculation time
1	2D	point / plane	12	1 days × 8 CPU's
2	2D	finite width	4 ... 18	0.5 ... 2 days × 8 CPU's
3	3D	finite width	120 ... 390	9 ... 22 days × 16 CPU's

Table 2: Summary of different simulation setups.

On the boundaries, of course, symmetry conditions are applied on the front and back planes of the narrow cylindrical sector and the centerline for the quasi-2D calculations. On the container and draft tube walls no-slip conditions hold for the liquid, but to avoid the need to resolve the viscous sublayer a single phase turbulent wall function for a smooth wall has been applied. Assuming that direct contacts between the bubbles and the walls are negligible, free-slip conditions hold for the gas phase on these walls. Except when the point source approximation is used, these settings also apply for the lower and side walls of the sparger, while the top surface of the sparger is an inlet for the gas where the gas mass flow rate is imposed. With the point source approximation this flow rate appears as a mass source in the grid cell where the inlet is located. The free water surface at the top of the column is modelled by a degassing condition in CFX ⁶³.

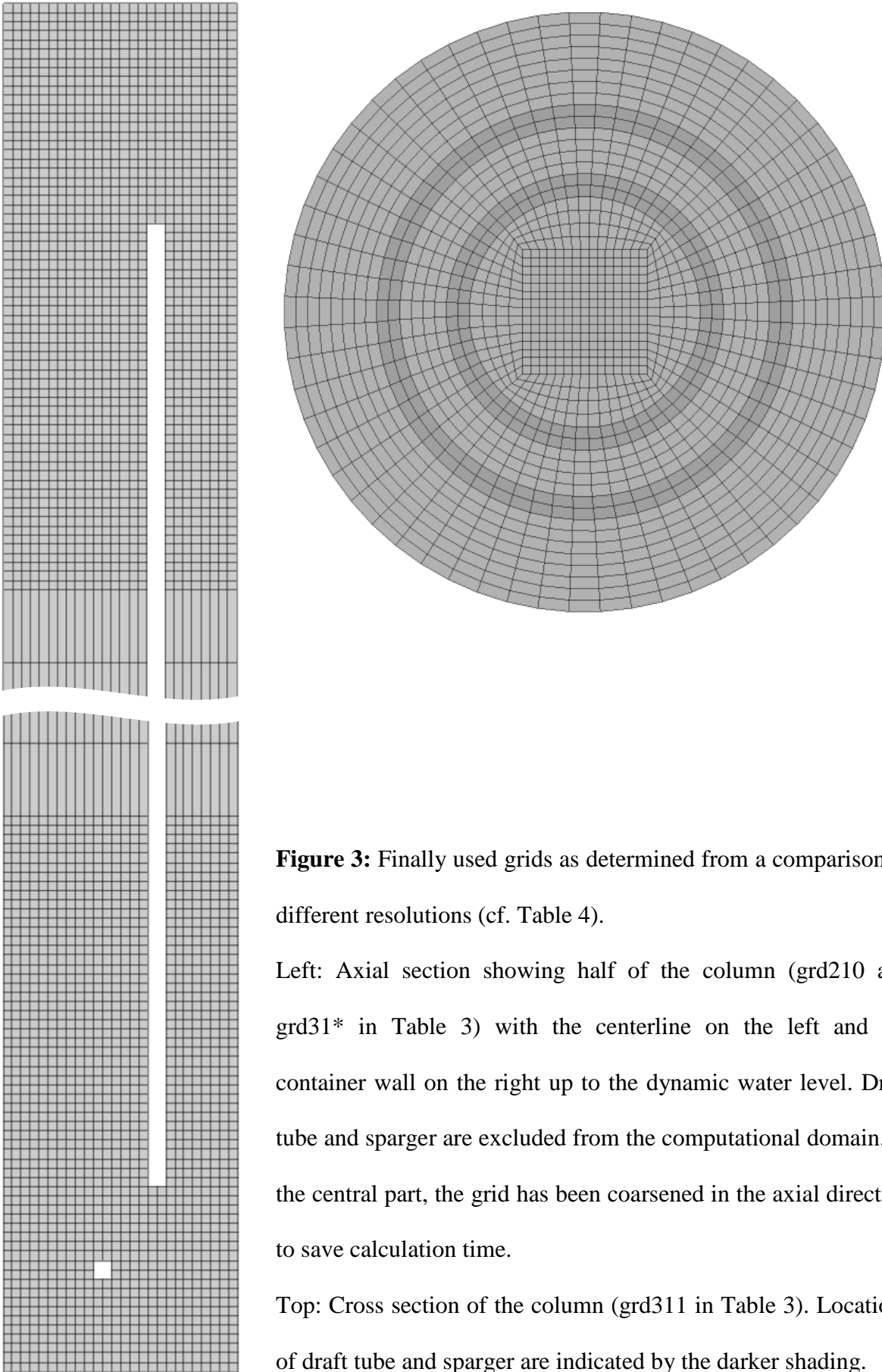


Figure 3: Finally used grids as determined from a comparison of different resolutions (cf. Table 4).

Left: Axial section showing half of the column (grd210 and grd31* in Table 3) with the centerline on the left and the container wall on the right up to the dynamic water level. Draft tube and sparger are excluded from the computational domain. In the central part, the grid has been coarsened in the axial direction to save calculation time.

Top: Cross section of the column (grd311 in Table 3). Locations of draft tube and sparger are indicated by the darker shading.

First attempts were made to run the simulations in stationary mode, but no convergence could be obtained. Therefore time-dependent simulations were run which revealed small oscillations of the gas fraction in the downcomer. It is not clear whether this represents actual physical behaviour that has not been resolved in the experiments or an artefact due to the approximations made in the modeling. To obtain unbiased values that can be compared with the experimental data, averaging over one period of these oscillations has been performed.

The bubble size appears in all of the correlations described in section 3 and hence is needed as input to the simulations. Since the origin of the reported value of 3 mm is not known and its reliability cannot be judged, it will be treated as a parameter. A monodisperse approximation is assumed where all bubbles have the same size. In reality of course a certain amount polydispersity is likely to be present, but considering the lack of data on the bubble size it does not appear fruitful to introduce additional unknowns by attempting to include this effect.

Air and water are treated as materials with constant properties at ambient conditions. Values used for the material properties are listed in Table 3.

ρ_L	997.0	kg m^{-3}
μ_L	8.899e-4	$\text{kg m}^{-1} \text{s}^{-1}$
ρ_G	1.185	kg m^{-3}
μ_G	1.831e-05	$\text{kg m}^{-1} \text{s}^{-1}$
σ	0.072	N m^{-1}

Table 3: Material properties for the air water system at atmospheric pressure and 25°C temperature.

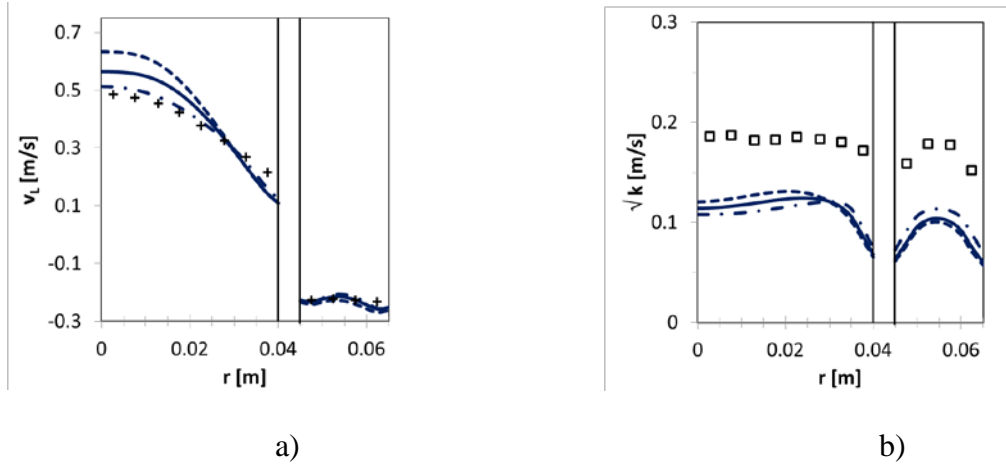
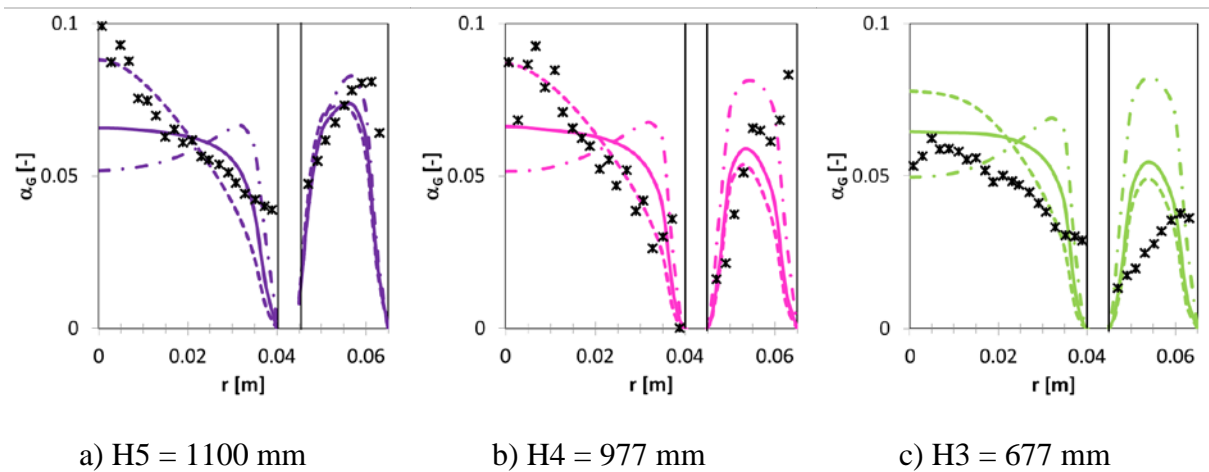


Figure 4: Comparison of simulation results using setup 2 (lines) and experimental data (symbols) for radial profiles of the axial liquid velocity (a) and the square root of turbulent kinetic energy (b). All data represent averages over 300-800 mm column height. The center of the column is on the left, its wall on the right, and the location of the draft tube is indicated by the vertical lines. Three values of the bubble size have been considered: $d_B = 5.5$ mm (dash-dotted), $d_B = 5.8$ mm (solid), and $d_B = 6.0$ mm (dashed).



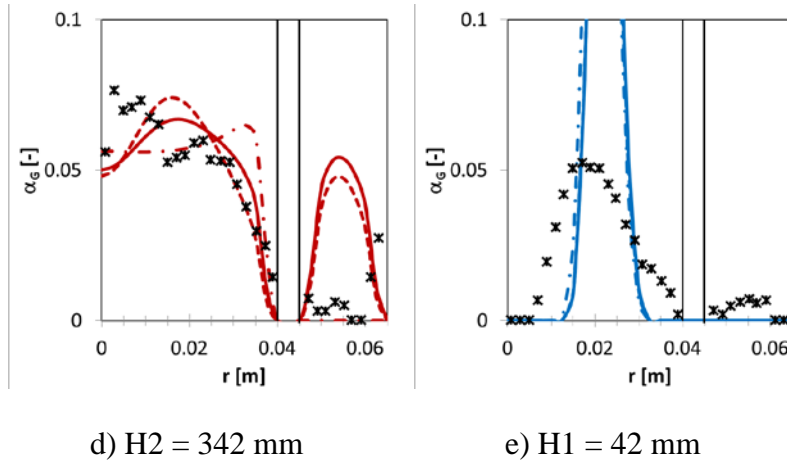


Figure 5: Comparison of simulation results using setup 2 (lines) and experimental data (symbols) for radial profiles of the gas fraction at the five measurement levels H1 through H5. The center of the column is on the left, its wall on the right, and the location of the draft tube is indicated by the vertical lines. Three values of the bubble size have been considered: $d_B = 5.5$ mm (dash-dotted), $d_B = 5.8$ mm (solid), and $d_B = 6.0$ mm (dashed).

Results on the effect of bubble size predicted by the baseline model described in section 3 are shown in Figure 4 and 5. Three values, 5.5, 5.8, and 6.0 mm have been chosen for the bubble size d_B , reasons for this choice will become obvious from the discussion. Setup 2 has been used to facilitate this parametric variation.

In Figure 4 radial profiles of the axial liquid velocity and the square root of turbulent kinetic energy as obtained from simulations using the different values for the bubble size (lines) are compared to the experimental data (symbols). Since the measured values represent averages over the height of column a corresponding average has also been applied to the simulation results. In the riser part of the column the liquid velocity has a parabolic profile which is well matched by the simulation results. Dependence on the bubble size is only weak. In the downcomer part of the column the liquid velocity is almost uniform. Again this is well matched by the simulation results. Dependence on the bubble size is negligible here. For the

square root of the turbulent kinetic energy the shape of the calculated profiles in both riser and downcomer parts of the column matches the data but the values are about a factor of two too low. Such discrepancies are in line with previous applications of the same baseline model to other systems^{39, 41-43} as well as other simulations of the present case³⁴. Since the understanding of turbulence is still far from complete even for single phase flows not more than this rough level of agreement can be expected.. Furthermore the possibility that the CARPT measurement technique significantly overestimates the velocity fluctuations has been noted by Luo³⁴. Dependence on the bubble size is again only weak.

In Figure 5 the gas fraction profiles at the five measurement levels as obtained from simulations using three different values for the bubble size (lines) are compared to the experimental data (symbols). The influence of the bubble size is most clearly seen in the riser part of the column. It stems from the dependence of the lift coefficient on the bubble size which changes its sign at a value of $d_B \approx 5.8$ mm. This means that smaller bubbles are driven towards the draft tube while larger bubbles are driven to the center of the riser. Correspondingly the calculated gas fraction profiles peak near the draft tube wall for $d_B = 5.5$ mm (dash-dotted) and in the center of the riser for $d_B = 6.0$ mm (dashed) while for $d_B = 5.8$ mm (solid) a rather flat profile is found. Considering that the baseline model has successfully described similar effects in bubbly pipe flows^{42, 43} and bubble columns⁴¹ the comparison with the measured gas fraction profiles suggest that the dominant fraction of bubbles has a size $d_B > 5.8$ mm. The strong effect of minute changes of the value chosen for the bubble size is most probably due to the monodisperse approximation whereas in reality a significant spread of bubble sizes is likely to be present. In the downcomer part of the column the liquid velocity profile is almost flat, so that no lift force is active and the main effect comes from the wall force which drives the bubbles towards the center of the downcomer..

Concerning the quantitative comparison between the simulation results and the measured data, the value of $d_B = 6.0$ mm gives a reasonably good agreement in the riser except at the lowest measurement level close to the inlet. It will be seen later on, that this issue is greatly alleviated by 3D simulations. In the downcomer the agreement is good only for the highest and lowest measurement level independent of the value used for the bubble size. The extent to which bubbles are carried downwards by the liquid, however, is not well captured in the simulations. Again this may be attributed to an effect of the polydisperse nature of the real flow which has been neglected in the simulations. Evidence from the literature^{45,8} suggests that the level to which bubbles are dragged down by the liquid flow depends on the bubble size. This dependence cannot be represented in a monodisperse simulation.

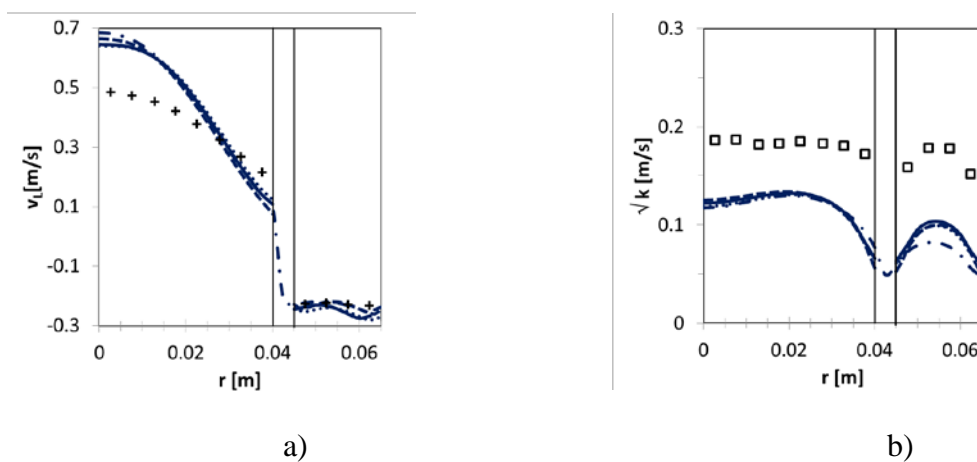


Figure 6: Comparison of simulation results for $d_B = 6.0$ mm and experimental data (symbols) for radial profiles of the axial liquid velocity (a) and the square root of turbulent kinetic energy (b). All data represent averages over 300-800 mm column height. The center of the column is on the left, its wall on the right, and the location of the draft tube is indicated by the vertical lines. Setup 2 has been considered with different grid resolutions (see Table 3): grd200 (solid), grd210 (dotted), grd220 (dashed). Setup 1: grd100 (dash-dotted).

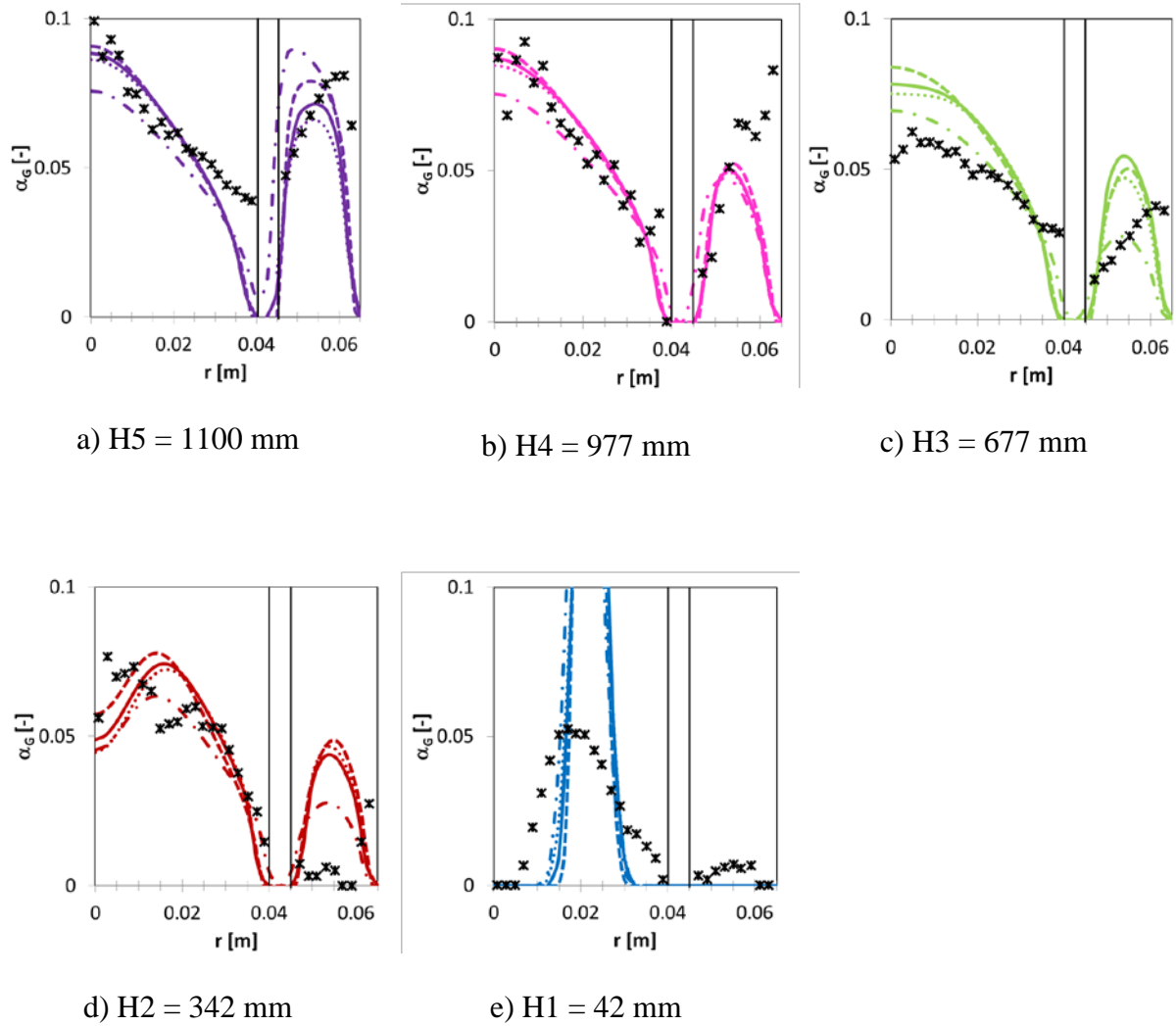


Figure 7: Comparison of simulation results for $d_B = 6.0$ mm and experimental data (symbols) for radial profiles of the gas fraction at the five measurement levels H1 through H5. The center of the column is on the left, its wall on the right, and the location of the draft tube is indicated by the vertical lines. Setup 2 has been considered with different grid resolutions (see Table 3): grd200 (solid), grd210 (dotted), grd220 (dashed). Setup 1: grd100 (dash-dotted).

A comparison of the quasi-2D simulations using different grid resolutions is shown in Figures 6 and 7. Only the value $d_B = 6.0$ mm which gave the best match to the measured data

has been used. Results show only small differences between the different grids used for setup 2 (solid, dotted, and dashed lines in Figs. 6 and 7) from which it may be concluded that grid independence has been achieved. In particular coarsening of the grid in the axial direction for the central part of the column (grd210) is shown to offer a good possibility to reduce the calculation time. Therefore this option has been used in the investigation of bubble size effects above. Simplification of the internals to lines and points in setup 1 (dash-dotted lines in Figs. 6 and 7) does affect the results to some extent, but the differences to the more accurate representation accounting for the finite extent of these internals are not overly large.

grid	setup	Δr	Δz	$\Delta\phi$	$N_{tot} / 10^3$
grd200	2	2.5 mm	2.5 mm	4°	11
grd210	2	2.5 mm	20 mm	4°	4
grd220	2	1.25 mm	7.5 mm	4°	18
grd100	1	2.5 mm	2.5 mm	4°	12
grd312	3	2.5 mm	20 mm	10°	120
grd311	3	2.5 mm	20 mm	6°	210
grd310	3	2.5 mm	20 mm	3.6°	390

Table 4: Summary of different grids. The setup refers to Table 2 where for the quasi-2D calculations a single grid cells is used in the azimuthal direction.

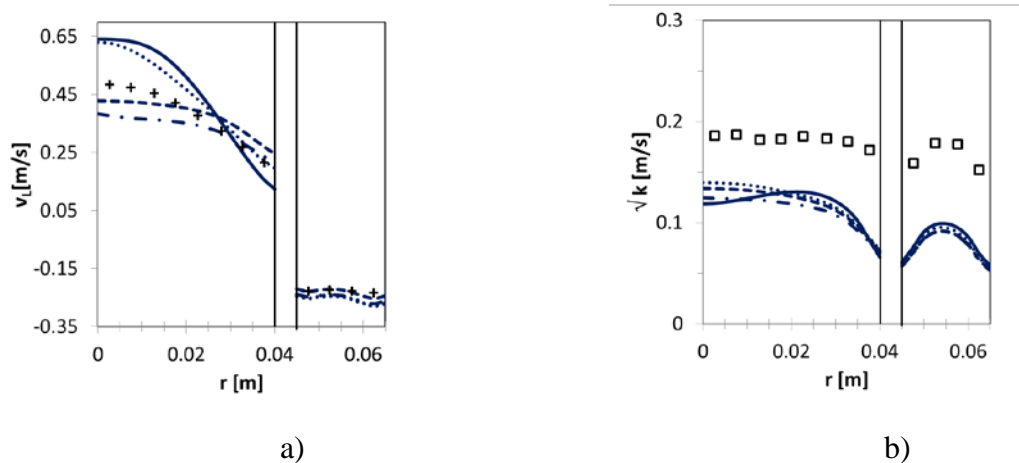
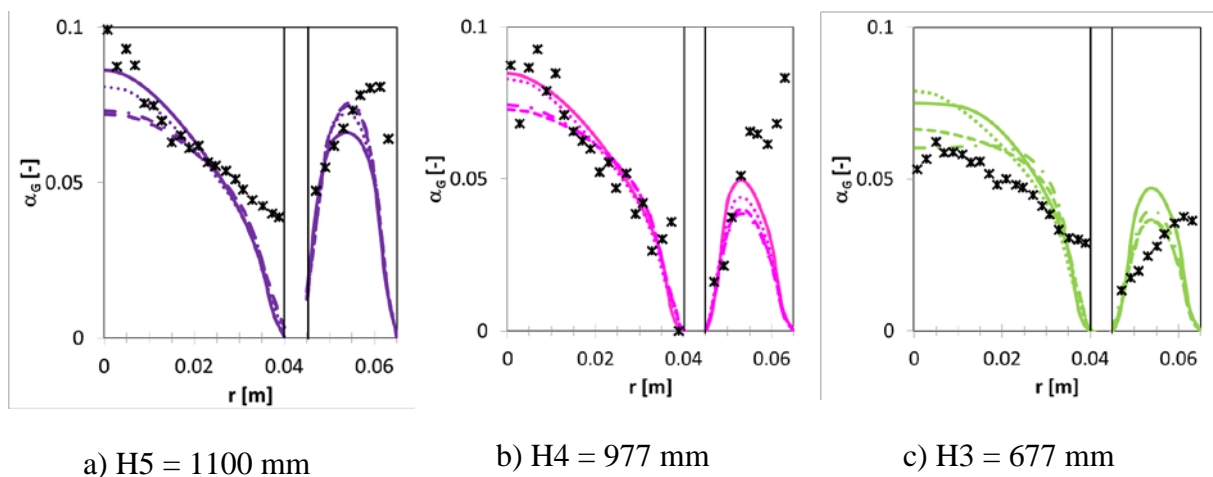


Figure 8: Comparison of simulation results for $d_B = 6.0$ mm and experimental data (symbols) for radial profiles of the axial liquid velocity (a) and the square root of turbulent kinetic energy (b). All data represent averages over 300-800 mm column height. The center of the column is on the left, its wall on the right and the location of the draft tube is indicated by the vertical lines. Setup 3 (3D) has been considered with different grid resolutions (see Table 3): grd312 (dotted), grd311 (dash-dotted), grd310 (dashed). Setup 2 (2D): grd210 (solid).



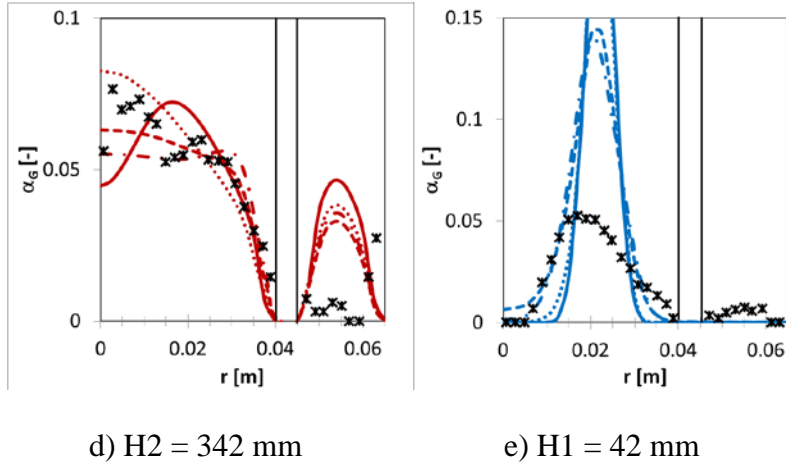


Figure 9: Comparison of simulation results for $d_B = 6.0$ mm and experimental data (symbols) for radial profiles of the gas fraction at the five measurement levels H1 through H5. The center of the column is on the left, its wall on the right and the location of the draft tube is indicated by the vertical lines. Setup 3 (3D) has been considered with different grid resolutions (see Table 3): grd312 (dotted), grd311 (dash-dotted), grd310 (dashed). Setup 2 (2D): grd210 (solid).

A comparison between 2D and 3D simulations is made in Figures 8 and 9. The solid lines give the result from the quasi-2D calculations discussed above. The dotted, dashed and dash-dotted lines give results for 3D calculations with different circumferential resolution of 36, 60, and 100 grid points. Coarsening in the axial direction is used for all computations. Results from the 3D simulations have been averaged azimuthally to facilitate comparison.

It is found that for the coarsest 3D grid the results are still very similar to those from the quasi-2D simulations, but as the circumferential resolution is increased differences appear. This indicates the importance of non-axisymmetric flow structures. For the two finest 3D grids the results agree, so that convergence with respect to the spatial discretization has been achieved and grd311 can be used for further investigations.

To illustrate the present non-axisymmetry a cross-sectional image of the gas distribution near the sparger is shown in Figure 10. A consequence of these non-axisymmetric structures is in particular that the peak in the gas fraction in the lowest measurement level near the inlet is greatly reduced, although a notable difference to the experiment still remains. In addition, the gas fraction and gas velocity profiles have become flatter in the center of the column. For the turbulent kinetic energy and in the downcomer region of the column differences are only small.

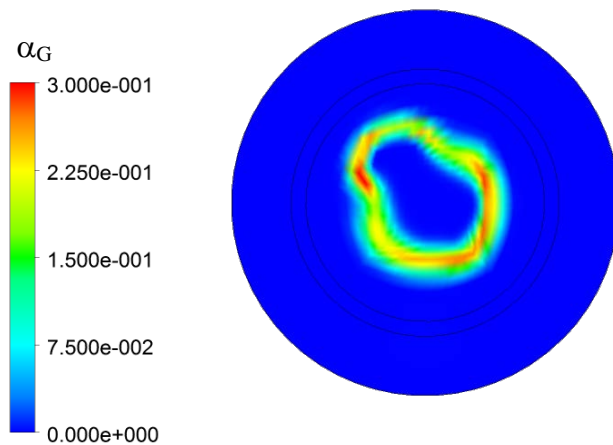


Figure 10: Cross-sectional distribution of gas fraction close to the inlet at $H_1=42\text{mm}$ from 3D simulations (grd310). The black lines indicate the location of the draft tube.

Since fluctuations are seen to be important for some aspects of the airlift-column fluid dynamics it is worthwhile to investigate also their contribution to the measured turbulent kinetic energy. As discussed by Ziegenhein et al.⁴¹ the turbulent kinetic energy in a transient URANS simulation consists of two contributions: (i) a resolved part which is obtained by

time-averaging the fluctuations of calculated velocity field and (ii) a modeled part which is obtained directly from the turbulence model. So far only the latter has been shown, but for a true comparison with experimental data both contributions should be added. Figure 11 shows the resulting total turbulent kinetic energy and the individual contributions for the 3D simulation. As can be seen the modeled contribution is by far the dominant one and adding the resolved contribution gives only a minor improvement in comparison with the experimental data.

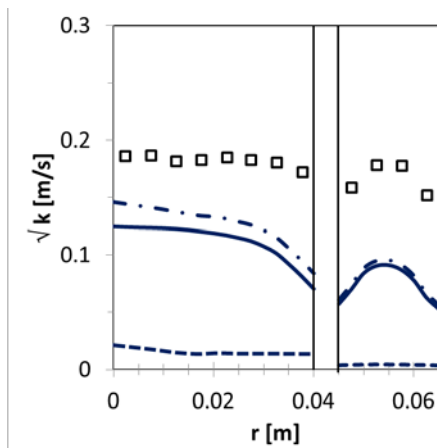


Figure 11: Square root of resolved (dashed line) and modeled (solid line) contributions to the total turbulent kinetic energy (dash-dotted line) from the 3D simulations on grd311 for $d_B = 6.0$ mm in comparison with the experimental data. All data represent averages over 300-800 mm column height.

The effects of adding the virtual mass force have been investigated for the final grids in both 2D and 3D setups (grd 210 and grd311). It is found small for all of the available data so no additional figure is shown.

4 DISCUSSION AND CONCLUSIONS

A baseline model previously validated for bubbly flows in pipes and bubble columns is found capable to describe also the flow in an internal loop airlift column with draft tube. Liquid circulation and gas fraction in the riser are captured well while the prediction of gas fraction in the downcomer and turbulent kinetic energy deserve further improvement.

In comparison with the simulations of Luo³⁴ of the same experiment, the performance of our approach is similar. In their simulations like in the present ones, the liquid circulation matched well with the measured data and the turbulent kinetic energy was strongly underpredicted. For the gas fraction only the middle level (H3) was considered in their comparison and the prediction of the simulations was too low compared with experiment, whereas here a reasonable match was found. Concerning the model the main difference is that Luo³⁴ neglected the lift force while we here include a model that accounts for the bubble deformation that has been successfully applied to several other validation cases.

The main shortcoming of the present calculations is the assumption of a monodisperse bubble size distribution which has been made in the absence of reliable data on the bubble size. Since the extent to which bubbles are dragged down into the downcomer depends on the bubble size^{45,8} this is the likely cause why the gas fraction in the downcomer is not well described. A polydisperse calculation⁶⁴ may be expected to improve thereon but to avoid introducing further unknown parameters experimental data on the bubble size distribution are required.

Concerning turbulence, the predictions might benefit from a full Reynolds stress model which should provide a better description of the top and bottom regions where the flow direction changes. The open question then is how to generalize the source terms for the bubble induced turbulence if the assumption of isotropy is relaxed.

Concerning the question which setups are suitable for the simulation of airlift columns the conclusion is that for highly accurate results, fully 3D simulations are necessary because fluctuations which are not axisymmetric play a significant role in particular near the gas inlet. If this region is not of special interest and some mild errors can be tolerated useful approximate results can also be obtained using a quasi-2D setup which greatly reduces the necessary computation times. A transient calculation has been found necessary in both cases to obtain a converged solution.

Concerning applications to biotechnological problems the next steps are inclusion of suitable models for the microorganisms as a third particle-like phase and the addition of mass-transfer. Both will be pursued in the future.

5 ACKNOWLEDGEMENT

This work has been partially carried out in the frame of a research project (GZ: RZ 11/1-1) within the DFG Priority Programme 1740: “Reactive Bubbly Flows” funded by the DFG.

6 NOMENCLATURE

Notation	Unit	Denomination
-----------------	-------------	---------------------

A_I	-	Interfacial area density
C_B	-	bubble-induced turbulence coefficient ((1981_Sato) model)
C_D	-	drag coefficient
C_L	-	lift coefficient
C_{TD}	-	turbulent dispersion coefficient
C_{VM}	-	virtual mass force coefficient
C_W	-	wall force coefficient
C_μ	-	shear-induced turbulence coefficient (k- ϵ model)
d_B	m	bulk bubble diameter
d_\perp	m	bubble diameter perpendicular to main motion
D	m	pipe diameter
Eo	-	Eötvös Number
F_D	N m^{-3}	drag force
F_L	N m^{-3}	lift force
F_{TD}	N m^{-3}	turbulent dispersion force
F_{VM}	N m^{-3}	virtual mass force
F_W	N m^{-3}	wall force
g	m s^{-2}	acceleration of gravity
G	$\text{kg s}^{-1} \text{m}^{-2}$	mass flux
H	m	height of test section
J	m s^{-1}	volumetric flux = superficial velocity
k	$\text{m}^2 \text{s}^{-2}$	turbulent kinetic energy
Mo	-	Morton Number

p	Pa	pressure
r	m	radial coordinate
Re	-	Reynolds number
s	m	hydrodynamic wall roughness
t	s	time
u	m s^{-1}	velocity
u_τ	m s^{-1}	friction velocity
U	m s^{-1}	velocity scale
V	m^3	volume
x	m	axial coordinate
y	m	distance to the wall
α	-	volume fraction
δ	m	viscous length scale
ε	$\text{m}^2 \text{s}^{-3}$	turbulent dissipation rate
μ	$\text{kg m}^{-1} \text{s}^{-1}$	dynamic viscosity
ν	$\text{m}^2 \text{s}^{-1}$	kinematic viscosity
ρ	kg m^{-3}	density
σ	N m^{-1}	surface tension
τ_w	N m^{-2}	wall shear stress

7 REFERENCES

1. Berzins, A., Toma, M., Rikmanis, M. and Viesturs, U., Influence of Micromixing on Microorganisms and Products. *Acta Biotechnologica* 21:155–170 (2001).
2. Garcia-Ochoa, F. and Gomez, E., Bioreactor scale-up and oxygen transfer rate in microbial processes: An overview. *Biotechnology Advances* 27:153–176 (2009).
3. Schmidt, F. R., Optimization and scale up of industrial fermentation processes. *Applied Microbiology and Biotechnology* 68:425–435 (2005).
4. Wu, B., Advances in the use of CFD to characterize, design and optimize bioenergy systems. *Computers and Electronics in Agriculture* 93:195–208 (2013).
5. Boyjoo, Y., Ang, M. and Pareek, V., Some aspects of photocatalytic reactor modeling using computational fluid dynamics. *Chemical Engineering Science* 101:764–784 (2013).
6. Bitog, J. P., Lee, I. B., Lee, C. G., Kim, K. S., Hwang, H. S., Hong, S. W., Seo, I. H., Kwon, K. S. and Mostafa, E., Application of computational fluid dynamics for modeling and designing photobioreactors for microalgae production: A review. *Computers and Electronics in Agriculture* 76:131–147 (2011).
7. Schmalzriedt, S., Jenne, M., Mauch, K. and Reuss, M., Integration of Physiology and Fluid Dynamics. *Advances in Biochemical Engineering/Biotechnology* 80:19–68 (2003).
8. Chisti, Y., Pneumatically agitated bioreactors in industrial and environmental bioprocessing: Hydrodynamics, hydraulics, and transport phenomena. *Applied Mechanics Review* 51:33–113 (1998).
9. Merchuk, J. and Gluz, M., Bioreactors, Air-lift Reactors. In *Encyclopedia of Bioprocess Technology: Fermentation, Biocatalysis, Bioseparation*, Ficklinger, M. C. and Stephen, W. D. (eds.), Wiley (1999).

10. Choi, K., Chisti, Y. and Moo-Young, M., Comparative evaluation of hydrodynamic and gas-liquid mass transfer characteristics in bubble column and airlift slurry reactors. *The Chemical Engineering Journal and the Biochemical Engineering Journal* 62:223–229 (1996).
11. Merchuk, J. C., Ladwa, N., Cameron, A., Bulmer, M., Berzin, I. and Pickett, A. M., Liquid Flow and Mixing in Concentric Tube Air- Lift Reactors. *Journal of Chemical Technology and Biotechnology* 66:174–182 (1996).
12. Gavrilesco, M. and Tudose, R., Concentric-tube airlift bioreactors part I: Effects of geometry on gas holdup. *Bioprocess Engineering* 19:37–44 (1998).
13. Gavrilesco, M. and Tudose, R., Concentric-tube airlift bioreactors part II: Effects of geometry on liquid circulation. *Bioprocess Engineering* 19:103–109 (1998).
14. Gavrilesco, M. and Tudose, R., 1998. Concentric-tube airlift bioreactors part III: Effects of geometry on mass transfer. *Bioprocess Engineering* 19, 175–178.
15. Merchuk, J., Contreras, A., Garcia, F. and Molina, E., Studies of mixing in a concentric tube airlift bioreactor with different spargers. *Chemical Engineering Science* 53,:709–719 (1998).
16. Merchuk, J., Ladwa, N., Cameron, A., Bulme, R. and Pickett, A., Concentric-tube airlift reactors: effects of geometrical design on performance. *AIChE Journal* 40:1105–1117 (1994).
17. Siegel, M. H. and Merchuk, J. C., Mass transfer in a rectangular air-lift reactor: Effects of geometry and gas recirculation. *Biotechnology and Bioengineering* 32:1128–1137 (1988).
18. Drew, D. A., and Passman, S. L., Theory of Multicomponent Fluids, *Springer* (1998).

19. Yeoh, G. H., and Tu, J. Y., Computational Techniques for Multiphase Flows - Basics and Applications. *Butterworth-Heinemann, Elsevier Science and Technology* (2010).
20. Ishii, M., and Hibiki, T., Thermo-fluid dynamics of two-phase flow. *Springer*, 2nd ed (2011).
21. Gumery, F., Ein-Mozaffari, F. and Dahman, Y., Characteristics of Local Flow Dynamics and Macro-Mixing in Airlift Column Reactors for Reliable Design and Scale-Up. *International Journal of Chemical Reactor Engineering* 7:1–45 (2009).
22. Mahadevan, R., Burgard, A. P., Famili, I., Dien, S. V. and Schilling, C. H., Applications of metabolic modeling to drive bioprocess development for the production of value-added chemicals. *Biotechnology and Bioprocess Engineering* 10:408–417 (2005).
23. Kraakman, N. J. R., Rocha-Rios, J. and van Loosdrecht, M. C. M., Review of mass transfer aspects for biological gas treatment. *Applied Microbiology and Biotechnology* 91:873–886 (2011).
24. Merchuk, J. C., Garcia-Camacho, F. and Molina-Grima, E., Photobioreactors Design and Fluid Dynamics. *Chemical and Biochemical Engineering Quarterly* 21:345–355 (2007).
25. Silva, M. K., d'Avila, M. A. and Mori, M., Study of the interfacial forces and turbulence models in a bubble column. *Computers and Chemical Engineering* 44:34–44 (2012).
26. Diaz, M., Montes, F. and Galan, M., Influence of the lift force closures on the numerical simulation of bubble plumes in a rectangular bubble column. *Chemical Engineering Science* 64:930–944 (2009).
27. Deen, N., Solberg, T. and Hjertager, B., Large eddy simulation of the Gas-Liquid flow in a square cross-sectioned bubble column. *Chemical Engineering Science* 56:6341–6349 (2001).

28. Hosokawa, S. and Tomiyama, A., Multi-fluid simulation of turbulent bubbly pipe flow. *Chemical Engineering Science* 64:5308–5318 (2009).
29. Politano, M., Carrica, P. and Converti, J., A model for turbulent polydisperse two-phase flow in vertical channels. *International Journal of Multiphase Flow* 29:1153–1182 (2003).
30. Troshko, A. A., and Hassan, Y. A., A two-equation turbulence model of turbulent bubbly flows. *International Journal of Multiphase Flow* 27:1965–2000 (2001).
31. Mudde, R. F. and van den Akker, H. E. A., 2D and 3D simulations of an internal airlift loop reactor on the basis of a two-fluid model. *Chemical Engineering Science* 56:6351–6358 (2001).
32. van Baten, J., Ellenberger, J. and Krishna, R., Hydrodynamics of internal air-lift reactors: experiments versus CFD simulations. *Chemical Engineering and Processing* 42:733–742 (2003).
33. Blazej, M., Glover, G. C., Generalis, S. and Markos, J., Gas-liquid simulation of an airlift bubble column reactor. *Chemical Engineering and Processing: Process Intensification* 43:137–144 (2004).
34. Luo, H.-P., Analyzing and Modeling of Airlift Photobioreactors for Microalgal and Cyanobacteria Cultures. PhD-thesis, *Washington University, St. Louis* (2005).
35. Talvy, S., Cockx, A. and Line, A., Modeling Hydrodynamics of Gas-Liquid Airlift Reactor. *AIChE Journal* 53:335–353 (2007).
36. Huang, Q., Yang, C., Yu, G. and Mao, Z.-S., Sensitivity Study on Modeling an Internal Airlift Loop Reactor Using a Steady 2D Two-Fluid Model. *Chemical Engineering and*

Technology 31:1790–1798 (2008).

37. Mohajerani, M., Mehrvar, M. and Ein-Mozaffari, F., CFD analysis of two-phase turbulent flow in internal airlift reactors. *Canadian Journal of Chemical Engineering* 90:1612–1631 (2012).
38. Ghasemi, H. and Hosseini, S. H., Investigation Of Hydrodynamics And Transition Regime In An Internal Loop Airlift Reactor Using CFD. *Brazilian Journal of Chemical Engineering* 29:821–833 (2012).
39. Rzehak, R., and Krepper, E., Closure models for turbulent bubbly flows: A CFD study. *Nuclear Engineering and Design* 265:701–711 (2013).
40. Rzehak, R., Krepper, E., Ziegenhein, T. and Lucas, D., A Baseline Model For Monodisperse Bubbly Flows. *10th International Conference on CFD in Oil & Gas, Metallurgical and Process Industries* (CFD2014), Trondheim, Norway (2014).
41. Ziegenhein, T., Rzehak, R., and Lucas, D., Transient simulation for large scale flow in bubble columns. *Chemical Engineering Science* 122:1–13 (2015).
42. Rzehak, R., and Krepper, E., Bubbly flows with fixed polydispersity: validation of a baseline closure model. *Nuclear Engineering and Design* 287:108–118 (2015).
43. Rzehak, R., Krepper, E., Liao, Y., Ziegenhein, T., Kriebitzsch, S. and Lucas, D., Baseline Model for the Simulation of Bubbly Flows. *Chemical Engineering and Technology* 38:1972-1978 (2015).
44. Rzehak, R., Krepper, E. and Lifante, C., Comparative study of wall-force models for the simulation of bubbly flows. *Nuclear Engineering and Design* 253:41–49 (2012).

45. Siegel, M., H., Merchuk, J., C. and Schugerl, K., Air-Lift Reactor Analysis: Interrelationships Between Riser, Downcomer, and Gas-Liquid Separator Behavior, Including Gas Recirculation Effects. *AIChE Journal* 32:1585–1596 (1986).
46. Rzehak, R., and Krepper, E., CFD modeling of bubble-induced turbulence. *International Journal of Multiphase Flow* 55:138–155 (2013).
47. Ishii, M., and Zuber, N., Drag coefficient and relative velocity in bubbly, droplet or particulate flows. *AIChE Journal* 25:843–855 (1979).
48. Tomiyama, A., Kataoka, I., Zun, I., and Sakaguchi, T., Drag Coefficients of Single Bubbles under Normal and Micro Gravity Conditions. *JSME International Journal B* 41:472–479 (1998).
49. Zun, I. The transverse migration of bubbles influenced by walls in vertical bubbly flow. *International Journal of Multiphase Flow* 6:583–588 (1980).
50. Tomiyama, A., Tamai, H., Zun, I., and Hosokawa, S., Transverse migration of single bubbles in simple shear flows. *Chemical Engineering Science* 57:1849–1858 (2002).
51. Schmidtke, M., Investigation of the dynamics of fluid particles using the Volume of Fluid Method. PhD-thesis, *University Paderborn* (2008) (in German).
52. Wellek, R.M., Agrawal, A.K., and Skelland, A.H.P., Shapes of liquid drops moving in liquid media. *AIChE Journal* 12:854–862 (1966).
53. Lucas, D. and Tomiyama, A., On the role of the lateral lift force in poly-dispersed bubbly flows. *International Journal of Multiphase Flow* 37:1178–1190 (2011).

54. Tomiyama, A., Sou, A., Zun, I., Kanami, N., and Sakaguchi, Effects of Eötvös number and dimensionless liquid volumetric flux on lateral motion of a bubble in a laminar duct flow. *Proc. 2nd Int. Conf. on Multiphase Flow*, Kyoto, Japan (1995).
55. Hosokawa, S., Tomiyama, A., Misaki, S., and Hamada, T., Lateral Migration of Single Bubbles Due to the Presence of Wall. *Proc. ASME Joint U.S.-European Fluids Engineering Division Conference, FEDSM 2002*, Montreal, Canada (2002).
56. Burns, A.D., Frank, T., Hamill, I., and Shi, J.-M., The Favre averaged drag model for turbulence dispersion in Eulerian multi-phase flows. *Proc. 5th Int. Conf. on Multiphase Flow, ICMF2004*, Yokohama, Japan (2004).
57. Auton, T., Hunt, J., and Prud'Homme, M., The force exerted on a body in inviscid unsteady non-uniform rotational flow. *Journal of Fluid Mechanics* 197:241–257 (1988).
58. Maxey, M. R., and Riley, J. J., Equation of motion for a small rigid sphere in a nonuniform flow. *Physics of Fluids* 26:883–889 (1983).
59. Magnaudet, J., Rivero, M., and Fabre, J., Accelerated flows past a rigid sphere or a spherical bubble Part 1: Steady straining flow. *Journal of Fluid Mechanics* 284:97–135 (1995).
60. Menter, F. R., Review of the shear-stress transport turbulence model experience from an industrial perspective. *International Journal of Computational Fluid Dynamics* 23:305–316 (2009).
61. Kataoka, I., Besnard, D. C. and Serizawa, A., Basic Equation of Turbulence and Modeling of Interfacial Transfer Terms in Gas-liquid Two-phase Flow. *Chemical Engineering Communications* 118:221–236 (1992).

62. Wilcox, D. C., *Turbulence Modeling for CFD*. DCW-Industries (1998).
63. ANSYS, 2012. ANSYS CFX-Solver Theory Guide Release 14.5. ANSYS Inc.
64. Liao, Y., Rzehak, R., Lucas, D. and Krepper, E., Baseline Closure Model for Dispersed Bubbly Flow: Bubble-Coalescence and Breakup. *Chemical Engineering Science* 122:336–349 (2015).